Check for updates

Energy Technology

Energy Technology
Generation, Conversion, Storage, Distribution

RESEARCH ARTICLE OPEN ACCESS

Homogenized Mechanical Modeling of Porous Anode Coating to Determine Swelling-Induced Stresses Under Operational Conditions

Hung Lin[1,2] | Burkhard Lewerich[2] | Edwin Knobbe[2] | Timo Danner[3,4] | Arnulf Latz[3,4,5]

[1]Faculty of Engineering, Computer Science and Psychology, Ulm University, Ulm, Germany | [2]Battery Cell Competence Centre, Bayerische Motoren Werke Aktiengesellschaft, Munich, Germany | [3]Institute of Engineering Thermodynamics, German Aerospace Centre (DLR), Stuttgart, Germany | [4]Helmholtz Institute Ulm for Electrochemical Energy Storage (HIU), Ulm, Germany | [5]Institute of Electrochemistry, Ulm University, Ulm, Germany

Correspondence: Hung Lin (hung.lin@uni-ulm.de)

Received: 22 May 2026 | **Revised:** 14 October 2026 | **Accepted:** 26 October 2026

Keywords: anode | coating | composite material | constitutive equation | design of experiments | finite element method | materials science | nanoindentation | porosity | swelling

ABSTRACT

Determining internal stresses in cylindrical lithium-ion batteries is crucial when silicon-based particles are added to the porous anode coating (PAC). A reliable homogenized constitutive model must be developed to capture both out-of-plane and in-plane mechanical properties of the PAC to perform efficient cell-level mechanical simulations where particle-resolved approaches are computationally impractical. We propose a complete, balanced, and cost-effective workflow designed for practical engineering applications. Out-of-plane properties are characterized by microindentation (MI) experiments, while a particle-resolved simulation-based design of experiments (DoE) serves as an efficient tool to determine the bulk in-plane behavior. Simulations indicate an effective Poisson's ratio of the PAC bulk in a range from 0.2 to 0.39, which contradicts the zero Poisson's ratio assumption in existing literature. Finally, these results are used to parameterize porous elastic and Drucker-Prager Cap (DPC) plastic models to estimate swelling stresses under fully constrained conditions. The model predicts out-of-plane stresses of 2.5–3.5 MPa and in-plane stresses of 1.5–2.5 MPa at 10% macroscopic swelling of the PAC, which align with empirical literature data. The proposed workflow demonstrates a highly balanced and readily deployable engineering methodology for a mechanical analysis on a cell level.

1 | Introduction

The automotive industry continues to push for higher energy densities, where the integration of high-capacity silicon-based particles in lithium-ion battery anodes has become a primary focus of cell development [1]. However, the substantial volume expansion of silicon during lithiation introduces severe internal mechanical stresses, which can compromise the structural integrity and cycle life of the cell [2, 3]. Cylindrical cell formats are increasingly favored in the automotive industry to counteract the issue of swelling as their rigid housing provides a highly constrained boundary condition (effectively "encastré") that successfully curbs macroscopic volumetric expansion [4, 5]. However, it also subjects internal components to intense multiaxial pressures.

Table 1 provides a summary of the operational stresses and swelling intensities measured across various cell formats and anode compositions. Predicting these stresses is essential for cell design; however, modeling an entire cylindrical cell at a particle-resolved scale remains computationally challenging due to the hundreds of layers and millions of particles involved. Consequently, there is a significant research interest in developing homogenized mechanical models, where the porous electrode coating is treated as a continuous material with effective bulk properties [22]. Such models drastically boost the computational efficiency and provide

This is an open access article under the terms of the Creative Commons Attribution License, which permits use, distribution and reproduction in any medium, provided the original work is properly cited.

© 2026 Bayerische Motoren Werke AG and The Author(s). *Energy Technology* published by Wiley-VCH GmbH.

TABLE 1 | Comparison of literature data on battery swelling-induced stresses.

Observable: stress (fixed thickness, then measure battery stress)							
Ref	**Yr.**	**Author**	**Sample**	**Anode**	**Condition**	**Observable**	**Value**
[6]	2014	Cannarella et al.	Pouch	Graphite	σ_{ini} = 0.05/0.5/5 MPa ➔fix t	Rev. pouch stress	0.5/0.75/1 MPa
[7]	2014	Cannarella et al.	Pouch	Graphite	σ_{ini} = 0.05 MPa ➔fix t	Rev. pouch stress	1 MPa
[8]	2016	Liu et al.	Pouch	Graphite	σ_{ini} = 0.05 MPa ➔fix t	Rev. pouch stress	0.6 MPa
[9]	2017	Louli et al.	Pouch	SiO + Gr	Fix thickness	Rev. pouch stress	~2 MPa
				Si alloy + Gr			~2 MPa
				Si–C + Gr			~2 MPa
[10]	2019	Louli et al.	Pouch	Graphite	Fix thickness	Rev. pouch stress	~0.5 MPa
				Si alloy + Gr (1:9)			~0.75 MPa
[11][a]	2019	Müller et al.	Pouch	Si–C	σ_{ini} = 0.08/0.42/0.84 MPa ➔fix t	Irrev. pouch stress	σ_{max} ~ 5 MPa
[12]	2021	Spingler et al.	Pouch	Graphite	σ_{ini} = 1 MPa ➔fix t	Rev. pouch stress	0.3 MPa
[13]	2021	Vidal et al.	Cylindrical cell	Si–C + Gr(500 mAh/g)	Stiff housing	Rev. radial stress	~4 MPa
Observable: swelling (fixed clamp pressure, then measure swelling strain)							
Ref	**Yr.**	**Author**	**Sample**	**Anode**	**Condition**	**Observable**	**Value**
[14]	2003	Lee et al.	Pouch	Gr	σ_{clamp} ≈1 MPa	Rev. pouch swelling	2 to 4%
[15]	2016	Riegeret al.	Pouch	Gr	—	Rev. pouch swelling	~2.5%
[16]	2017	Sauerteig et al.	Dilato-meter cell	Gr	σ_{clamp} = 80 kPa	Rev. stack swelling	~5%
[17][b]	2018	Sauerteig et al.	Prismatic	Gr	$E_{clamp,}$ = 1.0/12.7 MPa[c]	Rev. cell swelling	~0.22/0.18 mm
[18]	2021	Spingleret al.	Anode	Gr	σ_{clamp} = 150 kPa	Rev. anode swelling	~5%
[19][d]	2021	Daubinger et al.	Anode	Gr	—	Irrev. anode swelling	~10%
						Rev. anode swelling	~10%
[13]	2021	Vidal et al.	Pouch	Si–C + Gr(500 mAh/g)	σ_{clamp} = 0.1/1 MPa	Rev. pouch swelling	1.3%
			Anode		Estimation calculation	Rev. anode swelling	23.4%
[20]	2023	Wang et al.	Pouch	Gr	—	Rev. pouch swelling	1%
				SiO + Gr			4%
[21]	2025	Wan et al.	Pouch	SiO + Gr (4:15)	σ_{clamp} = 34/103/172 kPa	Rev. pouch swelling	4.0/0.9/0.8%

[a]Irreversible pouch stress during aging.
[b]The thickness of the cell housing was not revealed. Thus, displacement instead of strain is shown.
[c]The stiffnesses of the clamp are 1.0 and 12.7 MPa.
[d]Irreversible anode swelling due to formation.

a practical framework to determine the swelling-induced stresses within cells.

The homogenized mechanical modeling of electrode coatings generally serves two distinct research objectives. The first focuses on crash safety and impact analysis, where the primary interest lies in the large-scale plastic deformation and post-yield behavior during collision events. Initial elastic properties are less critical in such scenarios as the material enters the plastic regime almost instantaneously upon impact [23]. The second field addresses battery operational conditions characterized by lower stress–strain magnitudes and reversible loading profiles [24]. In this context, elastic responses are fundamental, while plastic properties remain essential to capture the "settling effect" observed during early cycles of battery operation [6]. Figure 1 illustrates that the electrode coating is significantly compressed during calendering; however, the microstructure may undergo stress relaxation and subsequent springback when the time between calendering and cell assembly is large. The electrode coating evolves toward a new mechanical state once cycling commences, which results in a stabilized cycle without plasticity, as is depicted in Figure 1b–d.

The potential of the Drucker-Prager Cap (DPC) plastic model [25, 26] to simulate battery operational conditions has been elegantly demonstrated in pioneering works of Ipers et al. [27] and Jiao et al. [28]. These studies provided a significant contribution by successfully implementing the DPC framework to capture the complex pressure-dependent consolidation of an electrode coating during swelling and cycling. Their results validated the robustness of this constitutive approach for cell-level mechanical analyses. However, while these models

21944296, 2026, 11, Downloaded from https://onlinelibrary.wiley.com/doi/10.1002/ente.70723 by Karlsruher Institut Fur Technologie, Wiley Online Library on [13/11/2026]. See the Terms and Conditions (https://onlinelibrary.wiley.com/terms-and-conditions) on Wiley Online Library for rules of use; OA articles are governed by the applicable Creative Commons License

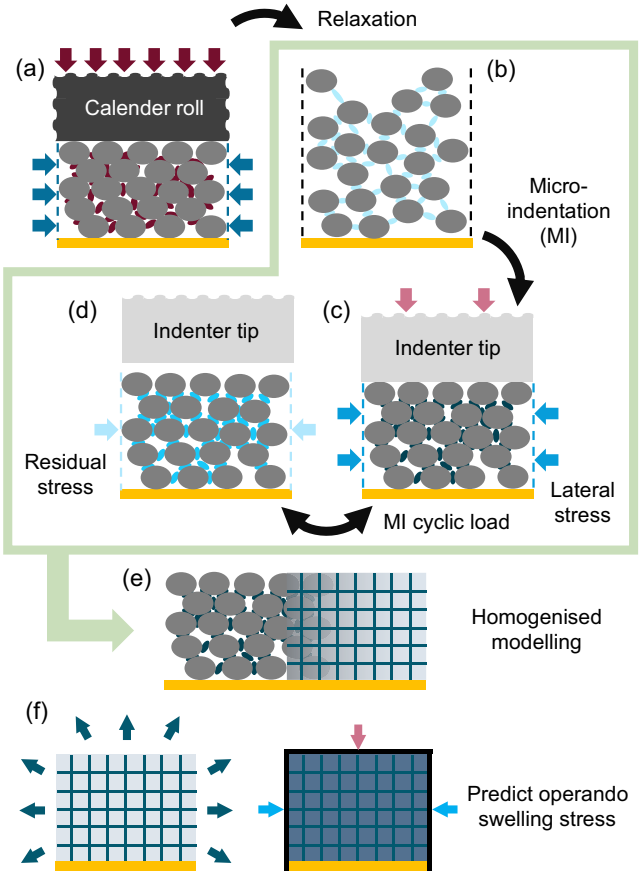


FIGURE 1 | Conceptual framework of the study. (a) The porous anode coating (PAC) layer gets calendered during manufacturing, which results in high normal and lateral stresses. (b) The PAC layer relaxes during transportation and storage. It springs back in normal direction and its lateral stress got relaxed. (c) The PAC undergoes cyclic loading by microindentation (MI) that emulates battery operational stresses. Lateral stress arise due to the uniaxial strain boundary condition. (d) Residual lateral stress occurs in the PAC bulk when the load is removed during cycling. (e) The objective of this research is to model (b), (c), and (d) with a homogenized mechanical model efficiently in a commercial tool to (f) predict bulk swelling-induced stresses under the encastré boundary condition typically found in a cylindrical cell during battery operations.

established a solid foundation for operational out-of-plane (normal) stress prediction, they largely adhered to the common assumption of negligible in-plane (lateral) stresses in a porous structure [28]. This specific assumption, while computationally convenient, may not fully represent the mechanical environment in high-constraint configurations, such as cylindrical cells. Consequently, it remains necessary to refine these established models by investigating the intrinsic lateral-to-normal stress coupling, which is one of the focuses of the current study.

Particle-based simulations offer a powerful alternative to investigate the intrinsic lateral-to-normal stress transmission that is challenging to measure experimentally. This potential is underscored by a vast body of discrete element method (DEM)-based literature focused on the calendering process [29]. For instance, Sonzogni et al. represented electrode particles as two-layer structures with a soft outer shell to capture realistic contact mechanics [30], while Lippke et al. used DEM to examine how diverse particle morphologies influence anode consolidation [31]. Beyond DEM, Foster et al. employed a particle-resolved finite element method (FEM) to study cathode mechanical behavior, achieving high alignment between simulated stress–strain data and experimental measurements [32]. Furthermore, Liao et al. successfully used particle simulations to derive the homogenized bulk response of an electrode coating [33]. Collectively, these studies demonstrate that particle-based approaches provide sophisticated means to explore mechanical properties; however, the characterization of lateral material behavior remains largely unaddressed. This gap highlights a significant opportunity to use these advanced numerical tools to investigate the multiaxial stress coupling within a porous anode coating (PAC).

In this study, we propose a complete, cost-effective workflow for material characterization and model parameterization to determine the internal operational stresses in a PAC. This workflow consists of four steps: first, the macroscopic normal mechanical properties of a PAC are characterized using cyclic compression tests in a Nanoindenter, which was proven to be versatile and cost-effective in a previous study [34]. Second, the effective lateral bulk material behavior of a PAC is investigated through particle-resolved FEM simulations. Third, the findings from the first two steps are combined to parameterize a macro-scale homogenized constitutive model. Finally, swelling simulations are done with the calibrated homogenized model under constrained boundary conditions to estimate swelling-induced stresses. This study focuses on obtaining a complete workflow, so each individual step prioritizes practical readiness as the core value lies in their balanced combination. In the first step, mechanical properties are not measured under various lithiated states. Instead, cyclic compression tests within the typical cell operating range are performed as a proxy to replicate operational dynamics and mechanical behavior during lithiation. In the second step, the complicated heterogeneous multiphase morphologies of a real PAC were neglected. Instead, particle-resolved simulations following a design of experiments (DoE) with well-defined idealizations are performed to ensure numerical reproducibility. Similarly, the parameterization in the third step uses well-established mechanical frameworks from the literature. The choice of the porous elastic [35] and DPC plastic [25, 26] models is well supported for electrode coatings, as demonstrated by the promising results of Brehm et al. [36] Jiao et al. [28] In addition, these classic constitutive frameworks are widely supported across commercial simulation packages, which ensures immediate engineering applicability and high replicability for practical cell-level simulations.

This article is structured as follows: the method section details the experimental setup, the particle-resolved simulation framework, the formulation of the selected homogenized model, and the setup of homogenized simulations to predict swelling-induced stresses. The results and discussion section presents the normal stress–strain curves, the effective range of bulk Poisson's ratios of a PAC, the parameterization process of the homogenized model, and the predicted swelling-induced stresses under constrained boundary conditions. Finally, the limitations and outlook of the workflow are discussed.

21944296, 2026, 11, Downloaded from https://onlinelibrary.wiley.com/doi/10.1002/ente.70723 by Karlsruher Institut Fur Technologie, Wiley Online Library on [13/11/2026]. See the Terms and Conditions (https://onlinelibrary.wiley.com/terms-and-conditions) on Wiley Online Library for rules of use; OA articles are governed by the applicable Creative Commons License

2 | Methodology

Figure 2a illustrates the comprehensive workflow with four sequential implementation steps: physical experiment (red), particle-resolved simulation (green), homogenized modeling (blue), and swelling-induced stress prediction (yellow). The role of each step and their connections are structured as follows: physical experiments characterize macroscale normal stress–strain profiles and the mechanical hysteresis under cyclic loading of a PAC. The particle-resolved simulation step evaluates how normal stresses are transmitted into lateral stresses under bulk compression, helping to determine the plausible range of effective bulk Poisson's ratios of a PAC. Although normal stress–strain curves and hysteresis are also properties of the particle-resolved simulation results, they are used exclusively for qualitative cross-validation against experimental data. The homogenized modeling step combines empirical normal properties and simulated lateral properties to parameterize the porous elastic and DPC plastic models. This calibration follows a similar structural methodology to that of Brehm et al. [36] and Jiao et al. [28] but operates under different microstructural assumptions specific to this work. Note that the experimental hysteresis is omitted from the final homogenized model. This is a deliberate simplification to maintain the workflow's primary focus on systemic integration and to ensure that the calibration process remains easily reproducible. Finally, this calibrated macroscale framework is applied to evaluate the cell-level operando swelling-induced stresses, completing the workflow from physical characterization to practical application.

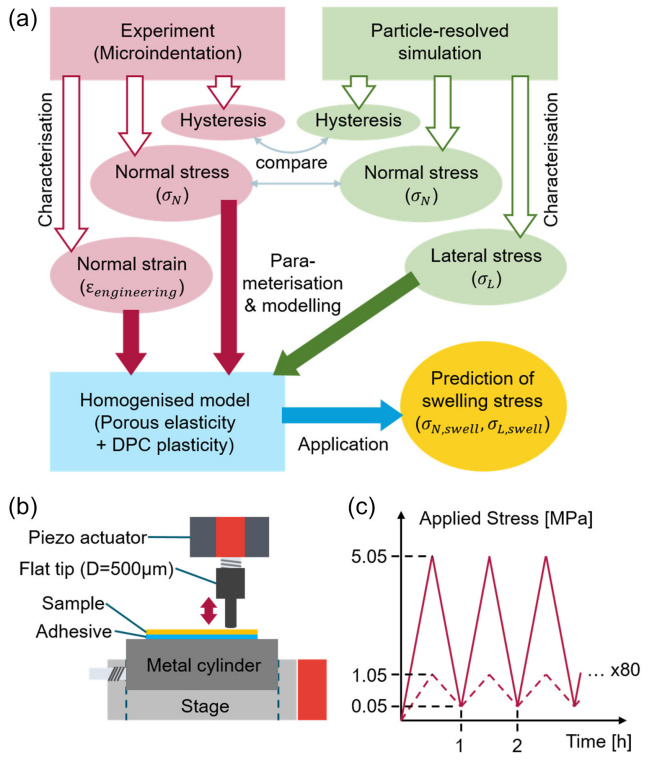


FIGURE 2 | (a) Overview of the workflow with experiments (red), particle-resolved simulations (green), homogenized modeling (blue), and application of predicting swelling-induced stresses (yellow). (b) Illustration of experimental setup with microindentation (MI). (c) Experimental load profile.

2.1 | Step 1: Physical Experiment

The physical experiments used microindentation (MI), as depicted in Figure 2b. A comprehensive description of this setup is provided in previously published work [34]; the critical feature is that the diameter of the flat indenter tip (D_{tip} = 500μm) is significantly larger than the particle size (D_{90} = 25μm) in a PAC. This ensures that the measured response represents the bulk average behavior of a PAC. Experimental load profiles, shown in Figure 2c, consist of two distinct cyclic loading regimes: one ranging from 0 to 1 MPa and another ranging from 0 to 5 MPa. Both maintain a 1 h periodicity repeated over 80 cycles. These intervals were selected to replicate stress cycles encountered during actual battery operations, as summarized in Table 1. Maximum observed stresses reach 5 MPa, while reversible stress fluctuations typically range between 0.3 and 4 MPa. A baseline load of 0.05 MPa was maintained to ensure full contact between the indenter and the sample surface. For brevity, these experimental conditions are referred to as the 1 MPa and 5 MPa cases.

The sample used in the experiments is an in-house-made single-side-coated anode. The copper foil was 10 μm thick. The composition of the PAC is 91% synthetic graphite, 6% Si–C, 3% aqueous binder, and <1% conductive additives. The specific capacity is 440 mAh/g, the loading is 10.8 mg/cm^2, and the thickness of the relaxed, calendered PAC layer before the experiments was 94 μm.

It is important to note that the experimental characterization was conducted on dry anode samples under compression levels representative of typical battery operations. In practice, the mechanical properties of a PAC may be altered by electrolyte wetting, while particle characteristics are subjected to changes during SEI formation and lithiation [37]. It is acknowledged that these dry-state results may not fully capture the complex in situ mechanical response of a PAC. This approach was adopted for this pioneering study to establish and validate the complete modeling workflow. Furthermore, specific parameter values may shift due to wetting or lithiation, but the fundamental nature of the mechanical constituent behavior remains consistent. Therefore, the proposed framework provides a robust foundation that can be subsequently refined with specific parameters for other states of the battery.

2.2 | Step 2: Particle-Resolved Simulation

Figure 3 illustrates the particle-resolved FEM used in this study, which will be referred to as the particle-resolved simulation. In this approach, individual particles are meshed, and contact algorithms are defined within a FEM framework in Abaqus [38]. This approach allows flexible adjustments to particle shapes and has significant potential to investigate changes in intrinsic particle properties, such as those occurring during lithiation or the shearing of graphite particles, that influence the bulk properties of a microstructure.

As shown in Figure 3a–c, the "domain of interest" (yellow frame) consists of a 50×50×50 μm^3 microstructure generated analytically with periodic boundary conditions using the software GeoDict [39]. The microstructure contains particles of identical shape and size for each individual simulation. Different microstructures were generated with different base particles to generate

21944296, 2026, 11, Downloaded from https://onlinelibrary.wiley.com/doi/10.1002/ente.70723 by Karlsruher Institut Fur Technologie, Wiley Online Library on [13/11/2026]. See the Terms and Conditions (https://onlinelibrary.wiley.com/terms-and-conditions) on Wiley Online Library for rules of use; OA articles are governed by the applicable Creative Commons License

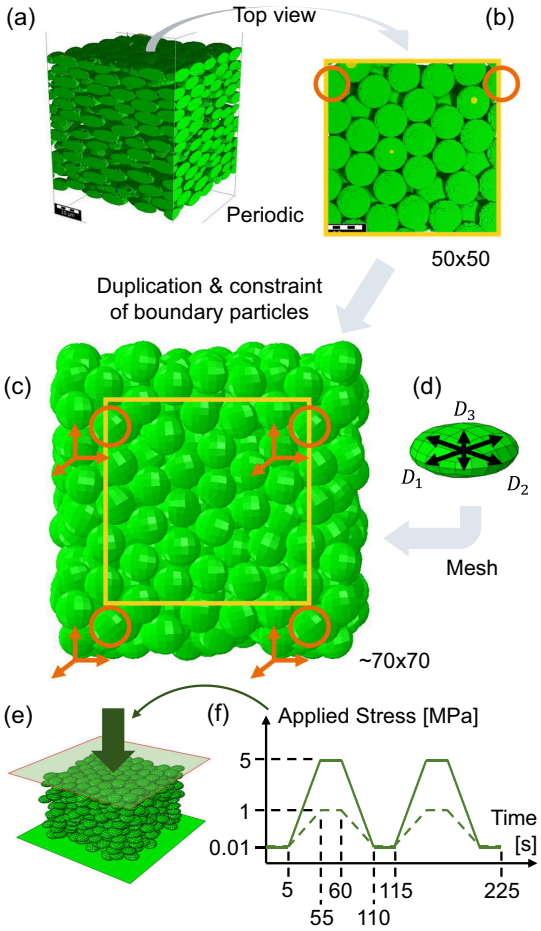


FIGURE 3 | Schematic illustration of the particle-resolved simulation. (a) Domain of interest (yellow frame): the periodic particle box generated in GeoDict. (b) Top view of the box. (c) Transfer the periodic box to a particle pile under an extended periodic boundary condition in Abaqus by duplicating and motion-linking the particles at the edge. (d) The mesh of a single 4×10×10 spheroid particle. (e) Domain of calculation in Abaqus under a bulk compressive load (all green spheroids). (f) The load profile used in the particle-resolved simulations.

various points in the DoE. The transition from the domain of interest to the Abaqus mesh is depicted in Figure 3b,c. To form the "domain of calculation," particles located at the periodic boundaries are duplicated into matching sets. Rigid-body motions and deformations of duplicated particles in each set are synchronized. This is achieved by enforcing identical nodal displacements across three corresponding, non-collinear reference nodes on each particle, effectively coupling their kinematic and deformational responses. For example, the four particles highlighted in orange in Figure 3c translate, rotate, and deform synchronously. This generates an extended periodic boundary condition. A minor trade-off of this method is that the two in-plane lengths of the calculation domain are slightly larger than the original domain of interest.

Bulk compression is applied to the particle assembly, as shown in Figure 3e, following the load profiles in Figure 3f. Two loading regimes are employed, sharing the same timing but differing in maximum stress. Each simulation begins with a 5 s hold at 0.01 MPa to ensure stable particle contact. The load was then increased to either 1 MPa or 5 MPa over 50 s, held for 5 s, and then unloaded back to 0.01 MPa over 50 s. This cycle was repeated twice. The time scale of these simulations differs from the physical experiments to accommodate the computational demands of explicit FEM simulations, which are not ideally suited for extremely long durations. Significant hysteresis within the microstructure is not expected because the viscosity of the binder is not modeled. This simplification makes such a loading applicable to our objectives.

The mechanical framework is defined by the constitutive law of particles and the interaction laws (contact and friction) at their interfaces. Abaqus version 2025 was used for all particle-resolved simulations. Detailed descriptions and explanations of used models are provided in Appendix A. Particles have identical linear elastic properties with a Young's modulus of 10 GPa and a Poisson's ratio of 0.3. The contact stiffness is fixed at 2 GPa, and particle penetration is permitted to simulate the binder elastic modulus and deformability [37]. This allows particles to act as "effective particles," representing an active material core covered by a deformable binder layer. Particle cohesion and viscosity are not considered in this study for the sake of model simplicity. This simplification does not significantly alter the predicted mechanical response as the focus remains on lateral behavior where transmission paths of compressive forces play the dominant role. This allows for a clearer analysis of microstructural interactions under typical battery operating conditions.

The primary variables investigated are the friction coefficient (0.2, 0.5, and 0.8) and particle geometry. The particle dimensions are defined by fixed diameters $D_1 = D_2 = 10$ μ m, while the polar diameter D_3 varies between 4, 6, 8, and 10 μm (Figure 3d). Orientation is critical for nonspherical particles, such as spheroids. The angle between the microstructure thickness axis and the particle polar axis had a uniform distribution between 0° and 5° during the generation of the microstructure. Although these orientations shift slightly during the initial 5 s of the simulation, the final state visually resembles calendered graphite anodes [40, 41]. To ensure repeatability, the same particle geometry was used to generate three different microstructures with different random seeds in GeoDict. This resulted in 12 unique microstructures (3 friction coefficients times 4 polar diameters) and a total of 36 simulations (12 microstructures times 3 seeds).

2.3 | Step 3: Homogenized Modeling

A macroscale homogenized constitutive model must properly couple the volumetric compaction with the evolving material stiffness to predict the swelling-induced stresses in a PAC in a constrained environment. A logarithmic porous elastic model is employed in this step of the workflow to capture the nonlinear elastic behavior of a PAC observed in our MI experiments. Its instantaneous stiffness depends on the current hydrostatic pressure because PAC is a granular porous structure. Within this framework, the purely elastic component of the material's volumetric change is defined to be proportional to the logarithm of the pressure stress [38]:

$$\frac{\kappa}{(1+e_0)}\ln\left(\frac{p_0+p_t^{\mathrm{el}}}{p+p_t^{\mathrm{el}}}\right)=J^{\mathrm{el}}-1 \tag{1}$$

21944296, 2026, 11, Downloaded from https://onlinelibrary.wiley.com/doi/10.1002/ente.70723 by Karlsruher Institut Fur Technologie, Wiley Online Library on [13/11/2026]. See the Terms and Conditions (https://onlinelibrary.wiley.com/terms-and-conditions) on Wiley Online Library for rules of use; OA articles are governed by the applicable Creative Commons License

Here, κ represents the logarithmic bulk modulus, e_0 is the initial void ratio, p is the current hydrostatic pressure, p_0 is the baseline initial pressure, p_t^{el} is the elastic tensile strength sustaining negative pressures, and J^{el} denotes the elastic volume ratio relative to the reference state.

The instantaneous shear modulus G is dynamically updated based on the current state of compaction to couple these shear responses with pressure-dependent volumetric behavior. The equivalent bulk Poisson's ratio ν identified from our particle-resolved simulation DoE is used to formulate the shear modulus as [38]:

$$G = \frac{3(1-2\nu)(1+e_0)}{2(1+\nu)\kappa}(p + p_t^{el})\exp(\varepsilon_{vol}^{el}) \tag{2}$$

where $\varepsilon_{vol}^{el} = \ln(J^{el})$ represents a logarithmic measure of the elastic volume change ratio. This constitutive formulation ensures that as the PAC is progressively compacted, the mechanical framework automatically self-adjusts both its bulk and shear resistances, aligning directly with our experimental results.

The DPC model is integrated into the framework to characterize settling effects observed during early battery cycling. Although originally developed for cohesive granular media, the dual-surface nature of the DPC model makes it exceptionally well suited for PACs, which exhibit strong pressure-dependent yield behavior. It incorporates a shear failure cone to capture shear-induced sliding and an adjustable plastic "cap" surface to govern volumetric material consolidation under severe compression.

In this workflow, the material response during swelling is predominantly driven by multiaxial compaction because the rigid housing of a cylindrical cell imposes a highly constrained boundary condition on a PAC. It is therefore assumed that the stress state sits safely within the compaction zone such that the transition surface between the shear failure cone and the consolidation cap can be omitted for efficiency reasons. Furthermore, the yield surface is assumed to be independent of the intermediate principal stress, forming a circular locus in the deviatoric plane. Under these workflow-specific assumptions, the shear failure cone is defined as [38]:

$$F_s = t - p\tan\beta - d = 0 \tag{3}$$

where t is the equivalent von Mises stress, p is the current hydrostatic pressure, and β and d denote the material's friction angle and cohesion, respectively. The elliptical cap yield surface in the meridional $(p-t)$ plane is formulated as [38]:

$$F_c = \sqrt{(p-p_a)^2 + (Rt)^2} - R(d + p_a\tan\beta) = 0 \tag{4}$$

to capture the irreversible compaction of the pore structure during lithiation-induced expansion. In this equation, R denotes a shape parameter that controls the eccentricity of the cap yield surface. The evolution parameter p_a, which determines the dynamic growth and expansion of the cap, is analytically related to the hydrostatic compression yield stress p_b via [38]:

$$p_a = \frac{p_b - \mathrm{Rd}}{1 + R\tan\beta} \tag{5}$$

The volumetric hardening law is explicitly governed by a piecewise linear function relating p_b directly to the accumulated volumetric plastic strain, which is parameterized using the residual plastic strains extracted from the stabilized experimental MI cycles.

To verify the framework and finalize this parameterization, homogenized compression simulations of MI load cases are performed under a specific normal loading profile consisting of two initial cycles between 0 and 1 MPa, followed by two sequential cycles between 0 and 5 MPa. A baseline pre-load of 0.01 MPa is strictly maintained during the unloading phases to ensure numerical stability within the FEM framework. Rate-dependent viscous features of the PAC are omitted in this constitutive step to align with the primary focus of the workflow on practical integration rather than standalone perfection of each individual part.

2.4 | Step 4: Prediction of Swelling-Induced Stresses

The calibrated homogenized model is applied to evaluate operando swelling-induced stresses under the encastré boundary conditions typical of cylindrical cells. Two extreme swelling scenarios are simulated. The first scenario is isotropic swelling, where volume expansion occurs identically in all directions, representing the behavior of near-spherical silicon particles with random orientations. The second scenario models one-dimensional (1D) swelling, where expansion is restricted strictly to a single thickness axis, representing the extreme macroscopic consequence of the highly aligned, flake-like morphology of the calendered graphite particles [40, 41].

The actual mechanical response of a real-blended PAC is assumed to fall naturally between these two physical limits. The proposed workflow successfully establishes a plausible numerical range for cell-level internal stresses by simulating both extremes without introducing overwhelming multiphase modeling complexity. In these simulations, element swelling is driven by a thermal framework in Abaqus. Consistent with the focus on workflow demonstration, the sole objective is to ensure that the ultimate free unconstrained volume expansion precisely matches our predefined target volumetric states. The specific choice of dummy thermal expansion coefficients and fictitious temperature boundary conditions does not alter the final macroscale equilibrium and is therefore not further detailed.

3 | Results and Discussion

The results of this study are structured according to the four steps of the workflow. The first step shows the normal mechanical properties of a PAC characterized by MI, followed by the effective lateral mechanical properties of a PAC determined by particle-resolved simulations. The third step presents the calibration of the homogenized model, followed by the fourth step, which presents the estimated swelling-induced stresses. Finally, the simplifying assumptions and limitations of the proposed framework are discussed.

21944296, 2026, 11, Downloaded from https://onlinelibrary.wiley.com/doi/10.1002/ente.70723 by Karlsruher Institut Fur Technologie, Wiley Online Library on [13/11/2026]. See the Terms and Conditions (https://onlinelibrary.wiley.com/terms-and-conditions) on Wiley Online Library for rules of use; OA articles are governed by the applicable Creative Commons License

3.1 | Mechanical Properties in Normal Direction

The red lines in Figure 4 show results from physical experiments. Dashed red lines indicate the first three cycles of the experimental cyclic load, while the solid red lines show the stabilized material response observed after approximately 20 h. Note that the results of the calibrated homogenized model from the third step are also plotted in Figure 4 to facilitate a direct comparison. A distinctive plastic behavior is evident during the initial cycle. For instance, in the 5 MPa experiment, the residual strain after the first unloading was approximately 0.065. Material creep is also observed as the maximum strain reached during the second loading cycle exceeds that of the first cycle, a trend that continues into the third cycle. We define this stage as the stabilization phase. After roughly 20 cycles (20 h), the stress–strain response forms a closed loop, as indicated by the red solid line. This suggests that the creep behavior has fully dissipated, leaving a pure elastic material. Note that a clear hysteresis remains, where the loading and unloading curves are distinctive. Supplementary tests (see Figure S1) at various load rates representative of normal battery operations revealed no significant changes in these loops. In fact, the loops at various load rates are almost identical, indicating that this is a rate-insensitive hysteresis in the considered stabilized states of PACs and loading conditions.

A comparison between the 1 MPa and 5 MPa experiments shows similar characteristics in both the initial creep and the subsequent stabilized loops. The primary distinction lies in the gradient of the first loading curve: the 1 MPa case appears softer than the 5 MPa case after reaching approximately 0.4 MPa. The most plausible explanation for this is that the loading rate in the 1 MPa experiment is five times slower than that in the 5 MPa experiment. It is physically consistent to observe a softer stress–strain curve at lower loading rates since viscous material responses are expected during the non-stabilized phase.

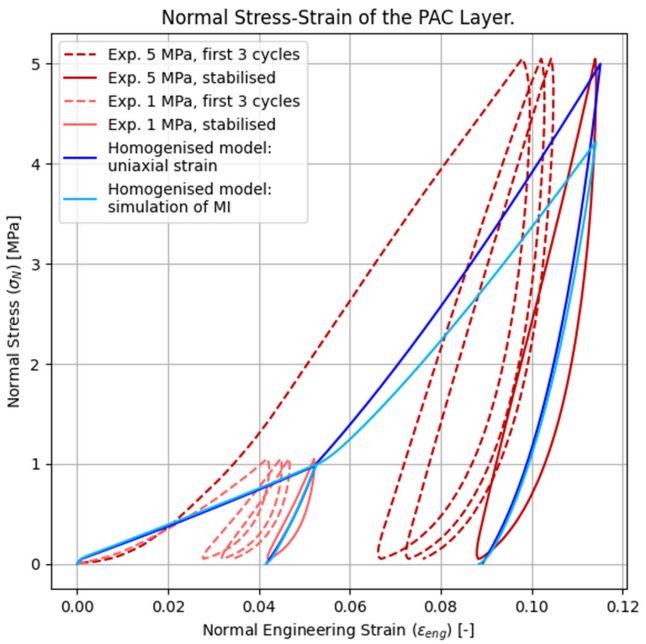


FIGURE 4 | The measurement results from experiments (red), the homogenized simulation result of the uniaxial strain load case (blue), and the homogenized simulation result of the measurement experiment (cyan).

3.2 | Mechanical Properties in Lateral Direction

The particle-resolved simulation results were compared with the physical experimental data from the previous step to assess their validity. Figure 5a,b display the stress–strain responses from the particle-resolved simulations (green curves). The simulations exhibit predominantly elastic behavior with a noticeable but moderate hysteresis loop. The red curves show the stabilized stress–strain response from the physical experiments. The immediate, predominantly elastic response observed in the particle-resolved simulations occurs because the generated initial microstructure already features pre-oriented particles and the target porosity. This dense initial state directly skips the early consolidation phase, closely resembling the fully stabilized condition of a cycled real PAC. Note that the resulting stress–strain magnitudes align closely with experimental observations, given that the mechanical properties were adopted from the literature (Young's modulus of 10 GPa for particles and compressive stiffness of 2 GPa for binders). Although the omission of binder viscosity leads to a smaller hysteresis when compared with physical measurements, the particle-resolved simulations successfully capture the fundamental mechanical characteristics of a PAC. This validates the workflow as a qualitative predictive tool and provides a robust foundation for more precise modeling when higher-fidelity experimental data becomes available. Figure 5a,b further demonstrate that the normal stress–strain response exhibits low sensitivity to both the friction coefficient and particle geometry within the investigated ranges.

The green curves in Figure 5c illustrate the lateral material behavior characterized by the particle-resolved simulations, specifically the lateral stress coefficient K as a function of normal stress. K is defined as follows:

$$K = \frac{\sigma_L}{\sigma_N}, \tag{6}$$

where σ_N and σ_L denote, respectively, the normal and lateral stress in the bulk. For granular materials, K is a more appropriate metric than Poisson's ratio ν, as it evolves dynamically during deformation. In the 1 MPa loading regime (dashed green curve), K remains constant during bulk compression but increases during unloading. While reloading curves are omitted for clarity, K typically returns to its initial loading level and remains stable. In the 5 MPa simulation, the constant K value during loading is identical to the 1 MPa case, while the increase during unloading is more pronounced (solid green curve). This rise in K during unloading is an intrinsic characteristic of granular bulk materials. We focus on the constant K value observed during loading to predict the swelling-induced stresses in a PAC, as the onset of swelling effectively acts as a compressive loading process.

Figure 5d presents the constant K values obtained for different particle polar diameters D_3 and friction coefficients f. As previously noted, each particle geometry was used to generate three distinctive microstructures using different random seeds. The points and error bars in the plot represent the mean and standard

21944296, 2026, 11, Downloaded from https://onlinelibrary.wiley.com/doi/10.1002/ente.70723 by Karlsruher Institut Fur Technologie, Wiley Online Library on [13/11/2026]. See the Terms and Conditions (https://onlinelibrary.wiley.com/terms-and-conditions) on Wiley Online Library for rules of use; OA articles are governed by the applicable Creative Commons License

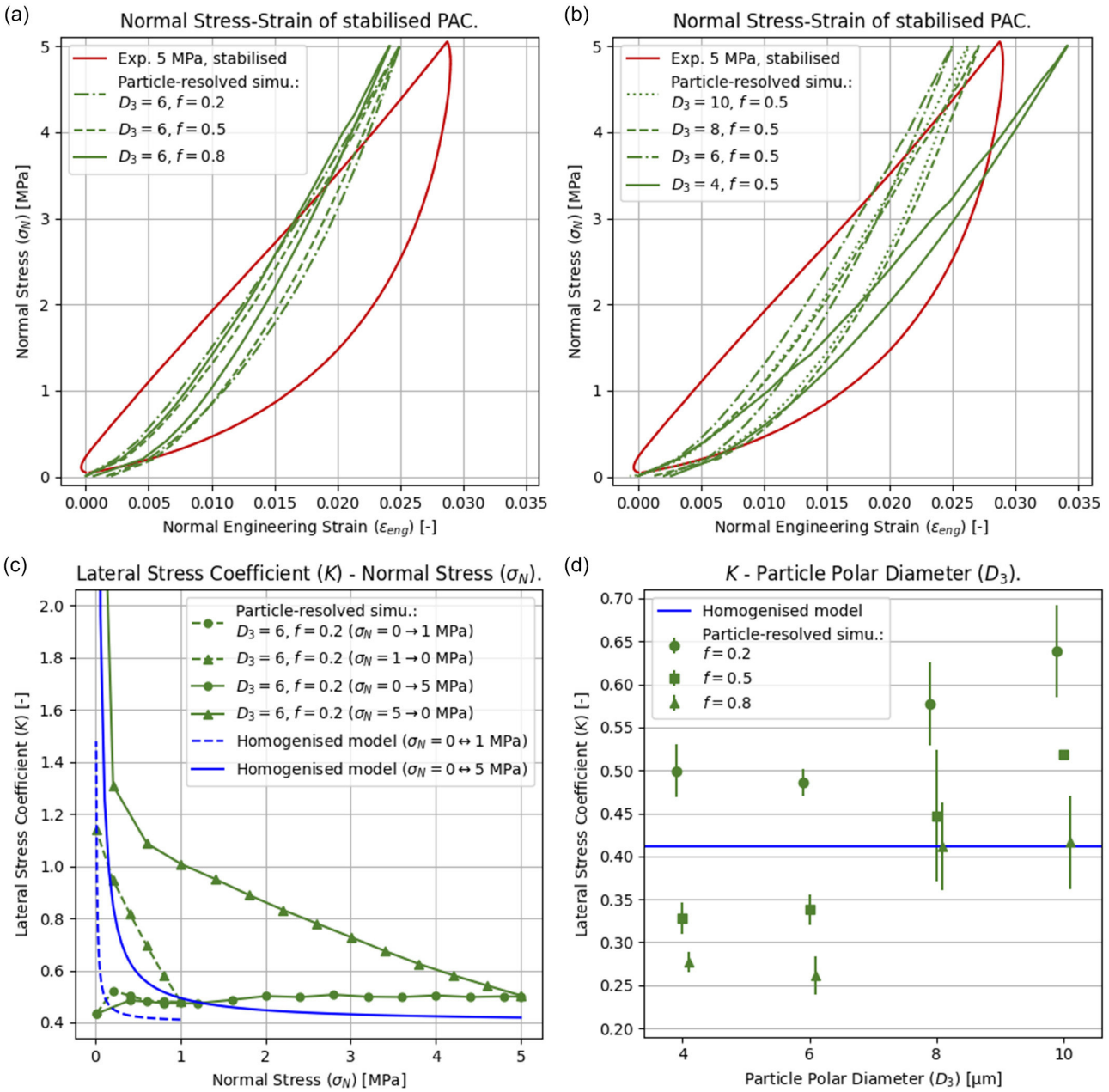


FIGURE 5 | (a) The normal stress–strain of particle-resolved simulation with different friction coefficients for particle–particle contact compared with experiment measurement after PAC stabilization. (b) is similar to (a) but with varying particle polar diameters instead of friction coefficient. (c) The lateral stress coefficient K during loading and unloading in particle-resolved simulations compared with the homogenized model. (d) The result of K over the complete design of experiment, and the selected value of K applied in the homogenized model, resulting in Poisson's ratio = 0.29.

deviation of K across these three realizations. The standard deviations are significantly smaller than the differences between the mean K values of different setups, except for the specific case of $D_3 = 8\,\mu m$ and $f = 0.5$. This suggests that the random seed has a negligible impact on the bulk properties; in other words, our "domain of interest" is sufficiently large to represent the characteristic lateral behavior of the microstructure. The higher variance for the case where $D_3 = 8\,\mu m$ and $f = 0.5$ suggests that this specific geometry is particularly prone to particle redistribution during compression. It appears that a friction coefficient of 0.5 acts as a critical threshold for this polar diameter, whereas at $f = 0.2$ or 0.8, the K values remain as stable as those of other particle geometries.

The friction coefficient significantly influences K, showing a consistent trend across all polar diameters, where a lower friction coefficient results in a higher K value. This can be explained by the fact that reduced friction facilitates particle redistribution, allowing normal stress to be more readily transmitted into lateral stress. The relationship between the polar diameter and K reveals further interesting insights. A noticeable decreasing trend in K is observed from $D_3 = 10\,\mu m$ down to $6\,\mu m$. However, at $D_3 = 4\,\mu m$, K slightly increases again. This nonlinear behavior suggests that K depends on a complex interplay between the polar diameter and the local geometric arrangement. The lateral force path is likely governed by the evolving particle–particle interactions at different aspect ratios.

21944296, 2026, 11, Downloaded from https://onlinelibrary.wiley.com/doi/10.1002/ente.70723 by Karlsruher Institut Fur Technologie, Wiley Online Library on [13/11/2026]. See the Terms and Conditions (https://onlinelibrary.wiley.com/terms-and-conditions) on Wiley Online Library for rules of use; OA articles are governed by the applicable Creative Commons License

The mean K values ranged from 0.25 to 0.65 across the tested ranges of polar diameters and friction coefficients. In a scenario of uniaxial strain elastic loading, this interval corresponds to an equivalent Poisson's ratio of $0.2 \leq \nu \leq 0.39$. Conclusively, the particle-resolved simulations allow us to estimate the plausible range of Poisson's ratio ν for a PAC and to observe its sensitivity to particle morphology.

3.3 | Calibration of the Homogenized Model

This step integrates the obtained empirical data from the first step and simulated lateral properties from the second step to calibrate the macroscale homogenized model. A median value of $\nu = 0.29$ was selected from the simulated range of Poisson's ratios to parameterize the logarithmic porous elastic model to represent the lateral behavior established in the previous step. The normal-direction properties were calibrated using the stabilized loading and unloading strain profiles from the 1 MPa and 5 MPa MI experiments. The initial void ratio e_0 was set to 0.5 based on electrode design, and the porous elastic parameters were then fitted at $\kappa = 0.025$ and $p_i^{el} = 0.6$ MPa. Finally, the irreversible plastic strains observed during these stabilized experimental cycles were used to parameterize the volumetric hardening law of the DPC plastic model as a piecewise linear function.

The remaining undefined parameters in the DPC plastic model are β, d, and R, as shown in Equations (3) and (4) . Under uniaxial strain conditions in our experiments, it is assumed that plastic deformation is driven solely by consolidation, i.e. yielding occurs exclusively on the cap. Rigid boundary conditions impose even higher lateral constraints, shifting the stress state further toward the hydrostatic axis on the meridional plane. The values $d = 0.05$ MPa and $\beta = 70°$ are selected in this work to ensure that the shear failure cone remains outside the stress states of interest while maintaining numerical stability.

Finally, the cap shape factor, R, was manually calibrated to satisfy two primary criteria. First, K was kept almost constant during the elastic and plastic (cap-yielding) regimes. Second, the residual lateral stress during unloading to 0.01 MPa was aligned with the estimations derived from the particle-resolved simulations. While it is acknowledged that our particle-resolved simulation primarily represents the stabilized elastic behavior and thus provides an approximation rather than a direct measurement, these results offer the most physically founded basis to estimate the residual stress state. Following this calibration, the R value was determined to be 0.62.

The blue curve in Figure 4 displays the normal stress–strain response of the homogenized model under uniaxial strain compression. The material undergoes plastic deformation during the initial loading from 0 to 1 MPa until it reaches the experimentally stabilized strain at 1 MPa, consistent with the model's parameterization. The model successfully recovers to the corresponding stabilized unloaded strain during unloading to 0.01 MPa. The model follows the previous unloading path during the subsequent loading cycle as no viscous effects or hysteresis loops are incorporated into this constitutive framework. This absence of hysteresis causes the main deviation from the experimental data. The curve follows the elastic path in the second phase during loading from 0 to 5 MPa before it reaches the previous yield threshold at 1 MPa, where it then exhibits a "kink" towards a softer response as cap yielding further develops. Predicting the initial plasticity of a PAC is vital to determine a realistic stress evolution in batteries. Finally, the model aligns with the experimental 5 MPa stabilized strain, with subsequent cycles remaining purely elastic.

The blue curves in Figure 5c illustrate the K of the homogenized model during cyclic compression after yielding. K follows a single path during both loading and unloading since the model is purely elastic after the initial yield and lacks hysteresis. Interestingly, this path appears to aggregate the loading and unloading trends observed in particle-resolved simulations: K is elevated at low normal stresses but decreases rapidly before stabilizing at a constant value as compression increases. Here, the blue curves of 0–1 MPa and 0–5 MPa are different because they are showing the value K of their stabilized states, respectively. In Figure 5d, the blue line indicates the constant K value of the homogenized model, which sits in the middle of the range of potential values identified by the particle-resolved study.

Figure 6a illustrates the meridional plane of the homogenized model under uniaxial strain. The stress state follows path A during initial loading from the pristine state to 5 MPa, where the cap-yield surface continuously evolves and "expands" to the right. A characteristic limitation of the built-in Abaqus DPC model is the constant cap eccentricity; consequently, the stress state follows path B upon unloading from 5 MPa and remains purely elastic within the newly established cap region. Any subsequently reapplied stress in this uniaxial configuration will follow path B, provided that the 5 MPa threshold is not exceeded.

Finally, the cyan curve in Figure 4 depicts the simulation of the physical MI experiment using the homogenized PAC model. In this setup, a 90 µm thick meshed PAC layer is compressed by an analytical rigid surface representing the flat indenter tip ($D_{tip} = 500$ µm). A divergence between the MI simulation and the ideal uniaxial strain case becomes noticeable beyond 1 MPa despite using identical material parameters. Acquiring additional stress–strain data in the 1–5 MPa range would enrich the calibration dataset, thereby elucidating why the deviation between the blue and cyan curves initiates precisely above 1 MPa. Nevertheless, the agreement remains sufficient for the qualitative scope of this study. The primary objective of the MI simulation was to demonstrate the robustness of the homogenized model; its numerical stability throughout the experimental loading profile suggests that it is well-suited for subsequent integration into complex cylindrical cell simulations.

Figure 6b illustrates the normal and lateral stress distribution in the PAC during a 5 MPa compression obtained by simulating the MI with the homogenized model. The stresses reach their maximum compressive value underneath the indenter. A transition zone is observed near the edge of the tip, with stresses gradually dissipating to zero at a certain distance beyond the contact boundary. The patterns of stress dissipation are different for normal and lateral stresses. This confirms that the "region of influence" of MI exceeds the actual tip dimensions, aligning with the conclusions of a previous work [34]. However, the influence region shown in Figure 6b is significantly smaller than the one predicted in our earlier study. This discrepancy originates from

21944296, 2026, 11, Downloaded from https://onlinelibrary.wiley.com/doi/10.1002/ente.70723 by Karlsruher Institut Fur Technologie, Wiley Online Library on [13/11/2026]. See the Terms and Conditions (https://onlinelibrary.wiley.com/terms-and-conditions) on Wiley Online Library for rules of use; OA articles are governed by the applicable Creative Commons License

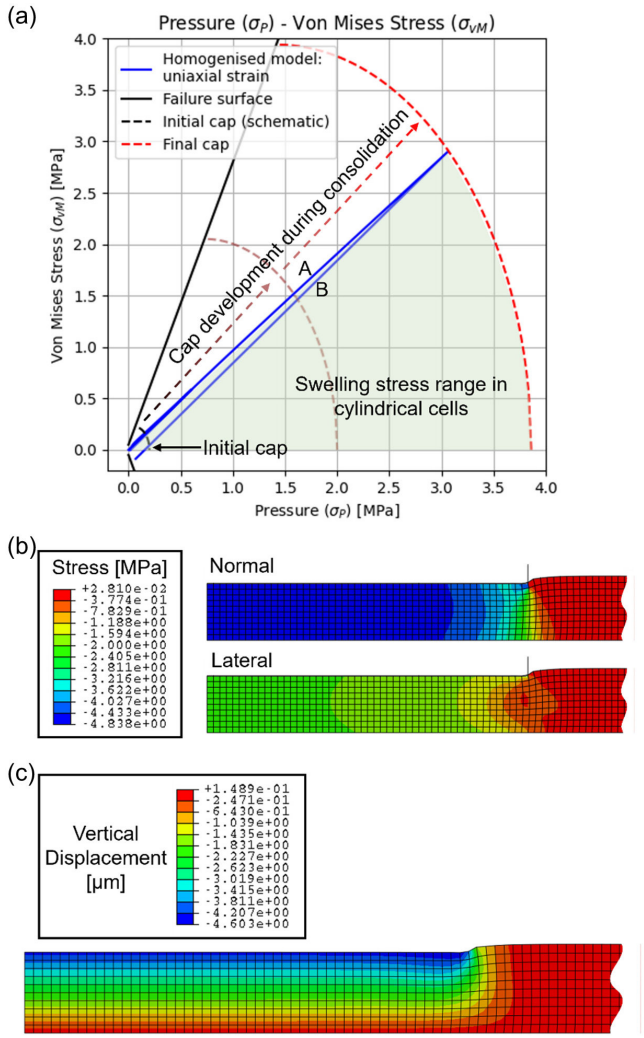


FIGURE 6 | (a) The uniaxial strain loading case on the meridional plane by the homogenized model. Path A and path B represents yielding and elastic loading of uniaxial strain load case. (b) Normal and lateral stresses of the PAC under compression predicted by the homogenized simulation of the MI experiment. (c) Plastic deformation predicted by the homogenized simulation of the MI experiment.

the estimation in the previous work based on a highly conservative methodology during the initial stage of workflow development. Given that PAC is a granular material, it cannot sustain high shear stresses at the edges of a tip. The more localized lateral stress distribution observed in this work is physically plausible. Furthermore, Figure 6c shows the residual deformation after unloading at 5 MPa. The plastic deformation profile appears equally reasonable, where the regions of influence identified from both the lateral stress and residual strain metrics show a clear alignment.

The rigid casing in a cylindrical cell imposes stronger lateral constraints, potentially leading to higher lateral stresses. This shifts the stress state into the green region, as shown in Figure 6a. This observation aligns well with our core assumption: the uniaxial strain case primarily induces consolidation-type yielding. Furthermore, it is physically plausible that a more hydrostatic stress state, such as the one found in a cylindrical cell, would further promote consolidation while suppressing the likelihood of shear failure during swelling. Consequently, the homogenized model, supported by the parameterization framework developed in this research, provides a logical and robust basis for predicting both normal and lateral stresses in cylindrical battery cells.

3.4 | Prediction of Swelling-Induced Stresses

Figure 7a,b illustrate the cases of, respectively, 1D-swelling and isotropic swelling and the corresponding stresses required to maintain a PAC in an encastré state. The normal and lateral stresses differ in the 1D swelling scenario, whereas they are identical under isotropic swelling. Figure 7c presents the relationship between the stress required when fully constrained and the volumetric expansion percentage of PAC when unconstrained. The hollow points indicate that the stress values were beyond the range of our physical characterization and were obtained by extrapolation.

According to Wang et al. [20] and Wan et al. [21], pouch cells containing silicon-based anodes exhibit up to 4% swelling during stabilized operation. Assuming this expansion is driven solely by anode lithiation, while neglecting cathode swelling and separator deformation, it could be estimated that the PAC itself undergoes approximately 10% volumetric expansion when it is assumed that the thicknesses of the cathode and anode layers are similar. Our homogenized simulations with encastré boundary conditions resulted in a range for normal stresses in the PAC between 2.5 and 3.5 MPa under this representative baseline of 10% free volume expansion. The lateral stress ranged between 1.5 and 2.5 MPa, which depends on the anisotropy of the swelling. This magnitude of stress matches the reported reversible radial stress of approximately 4 MPa for a cylindrical cell with a silicon-containing anode by Vidal et al. [13]. It is emphasized that Table 1 serves strictly as a macroscale, order-of-magnitude physical reference rather than a platform for direct quantitative benchmarking. Precise stress values are highly sensitive to specific electrode parameters. The goal of this research is not to achieve a perfect match for a single material but to validate the robustness of the integrated workflow. The alignment between the predicted stress magnitude and literature data demonstrates that by stitching physical experiments and simulative DoEs together, the proposed workflow delivers a practical and computationally efficient engineering framework to determine internal cell stresses under constrained conditions.

3.5 | Discussion and Framework Limitations

This study focuses on delivering a balanced workflow. Its modular structure allows individual steps to be independently updated as better testing methods or higher-fidelity data become available without altering the general framework.

First, regarding the experimental characterization, the current physical measurements were conducted on dry, unlithiated samples to establish the baseline workflow. To achieve higher accuracy, future work could extend these MI tests to electrolyte-wetted or progressively lithiated electrode samples

21944296, 2026, 11, Downloaded from https://onlinelibrary.wiley.com/doi/10.1002/ente.70723 by Karlsruher Institut Fur Technologie, Wiley Online Library on [13/11/2026]. See the Terms and Conditions (https://onlinelibrary.wiley.com/terms-and-conditions) on Wiley Online Library for rules of use; OA articles are governed by the applicable Creative Commons License

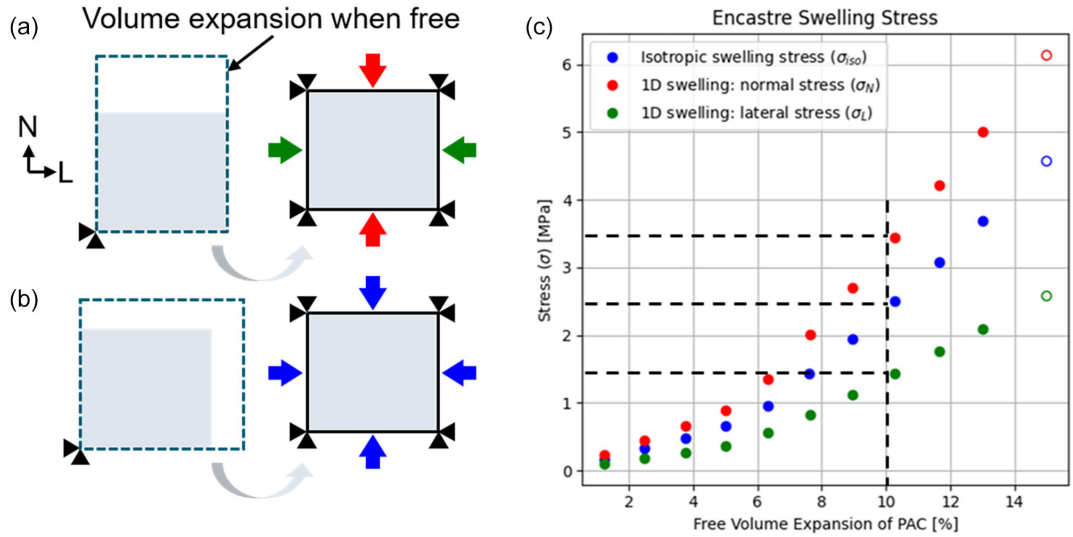


FIGURE 7 | (a) Schematic illustration of 1D-swelling. Normal and lateral stresses are needed to hold the initial geometry. (b) Schematic illustration of isotropic swelling. Pressure is needed to hold the initial geometry. (c) Prediction of the operando swelling stress by the homogenized model.

as the mechanical properties of active particles evolve significantly during cycling. Any refined stress–strain relationships can be directly used in our workflow to further improve the prediction.

Second, the particle-resolved simulation step can be advanced by transitioning from single-morphology idealizations to heterogeneous multiphase simulations. Future efforts could explicitly incorporate distinct graphite and Si–C phases into the random packing microstructures, assigning separate morphology laws and contact properties to individual particle types. This would allow a more detailed investigation into how the geometric interplay between flake-like and spherical particles alters the lateral force transmission pathways, further narrowing down the plausible range of bulk Poisson's ratios.

Third, the macroscale homogenized model calibration presents clear limitations when scaling up to an actual cylindrical jelly roll. In a real curved geometry, the mechanical impedance mismatch and layer-wise incompliance between the components will inevitably generate substantial interfacial shear stresses. The current framework is limited in its ability to capture these multiaxial shear interactions or potential interlayer slippage because our DPC shear failure cone was set intentionally high ($\beta = 70°$) for numerical stability and focused exclusively on compression-driven consolidation.

Finally, using industry-standard constituent models allows for efficient engineering implementation, which is essential for preserving the practical readiness of the overall workflow across various simulation platforms. However, these standard frameworks naturally simplify specific microstructural dissipative effects. Future refinements should therefore focus on transitioning towards more customized material models (e.g., UMAT in Abaqus) and designing dedicated multiaxial testing setups to precisely characterize both the shear failure locus and the hysteresis mechanisms. While requiring significantly more development and verification work, these advanced formulations represent a critical next step to bridge the gap between this fundamental framework and fully resolved 3D cell-level structural simulations of battery cells.

4 | Conclusion

In this study, a complete, balanced, and integrated workflow combining physical experiments, particle-resolved simulations, and homogenized modeling was demonstrated to determine the internal swelling-induced stresses of PACs. Experimental results demonstrate that PAC exhibits a non-linear stress–strain response, reaching a maximum measured strain of near 0.12 at 5 MPa, and displays distinct rate-insensitive hysteresis alongside a significant consolidation phase. Crucially, a particle-resolved simulation of DoE indicates that the effective bulk Poisson's ratio of PACs ranges between 0.2 and 0.39, providing a more accurate mechanical description than the common assumption of zero lateral stress in porous electrodes.

Based on these integrated findings, a standard homogenized mechanical model was parameterized using well-established porous elasticity and DPC plasticity models. While the experimental hysteresis was deliberately omitted to maintain the workflow's primary focus on straightforward integration and ease of replicability, the calibrated framework successfully simulated the complex MI loading case with high numerical stability. The framework predicts a normal swelling-induced stress range of 2.5–3.5 MPa and a lateral stress range of 1.5–2.5 MPa when applied to encastré boundary conditions typical of cylindrical cells. These results align closely with empirical radial stress measurements in the existing literature, confirming the model's reliability for cell-level mechanical analysis. Ultimately, this integrated, cost-effective parameterization workflow provides battery engineers with a highly adaptable and readily deployable methodology to evaluate internal mechanical loads, successfully bridging the gap between microscale granular properties and macroscale cell-level design.

21944296, 2026, 11, Downloaded from https://onlinelibrary.wiley.com/doi/10.1002/ente.70723 by Karlsruher Institut Fur Technologie, Wiley Online Library on [13/11/2026]. See the Terms and Conditions (https://onlinelibrary.wiley.com/terms-and-conditions) on Wiley Online Library for rules of use; OA articles are governed by the applicable Creative Commons License

Acknowledgments

The authors appreciate the kindness of their BMW colleague Dr. Manfred Rapp for providing the anode samples and extend their sincere thanks to colleagues at HIU and BMW for their insightful discussions.

Open Access funding enabled and organized by Projekt DEAL.

Funding

No public funding was received for this study.

Conflicts of Interest

The authors declare no conflicts of interest.

Data Availability Statement

The data that support the findings of this study are available from the corresponding author upon reasonable request.

References

1. M. Spielbauer, M. Steinhardt, J. Singer, A. Aufschläger, O. Bohlen, and A. Jossen, "Influence of Breathing and Swelling on the Jelly-Roll Case Gap of Cylindrical Lithium-Ion Battery Cells," *Batteries* 9 (2023): 6.

2. H. Jia, X. Li, J. Song, et al., "Hierarchical Porous Silicon Structures With Extraordinary Mechanical Strength as High-Performance Lithium-Ion Battery Anodes," *Nature Communications* 11 (1) 2020), 1474.

3. Y. Wang, M. Satoh, M. Arao, M. Matsumoto, H. Imai, and H. Nishihara, "High-Energy, Long-Cycle-Life Secondary Battery With Electrochemically Pre-Doped Silicon Anode," *Scientific Reports* 10, no. 1 (2020), 3208.

4. S. Baazouzi, N. Feistel, J. Wanner, I. Landwehr, A. Fill, and K. P. Birke, "Design, Properties, and Manufacturing of Cylindrical Li-Ion Battery Cells—A Generic Overview," *Batteries* 9 (2023): 309.

5. E. Feyzi, M. R. AK, X. Li, S. Deng, J. Nanda, and K. Zaghib, "A Comprehensive Review of Silicon Anodes for High-Energy Lithium-Ion Batteries: Challenges, Latest Developments, and Perspectives," *Next Energy* 5 (2024): 100176.

6. J. Cannarella and C. B. Arnold, "Stress Evolution and Capacity Fade in Constrained Lithium-Ion Pouch Cells," *Journal of Power Sources* 245 (2014): 745–751.

7. J. Cannarella and C. B. Arnold, "State of Health and Charge Measurements in Lithium-Ion Batteries Using Mechanical Stress," *Journal of Power Sources* 269 (2014): 7–14.

8. X. M. Liu and C. B. Arnold, "Effects of Cycling Ranges on Stress and Capacity Fade in Lithium-Ion Pouch Cells," *Journal of the Electrochemical Society* 163 (2016): A2501–A2507.

9. A. J. Louli, J. Li, S. Trussler, C. R. Fell, and J. R. Dahn, "Volume, Pressure and Thickness Evolution of Li-Ion Pouch Cells With Silicon-Composite Negative Electrodes," *Journal of the Electrochemical Society* 164 (2017): A2689–A2696.

10. A. J. Louli, L. D. Ellis, and J. R. Dahn, "Operando Pressure Measurements Reveal Solid Electrolyte Interphase Growth to Rank Li-Ion Cell Performance," *Joule* 3 (2019): 745–761.

11. V. Müller, R.-G. Scurtu, K. Richter, et al., "Effects of Mechanical Compression on the Aging and the Expansion Behavior of Si/C-Composite|NMC811 in Different Lithium-Ion Battery Cell Formats," *Journal of the Electrochemical Society* 166 (2019): A3796–A3805.

12. F. B. Spingler, S. Friedrich, S. Kücher, S. Schmid, D. López-Cruz, and A. Jossen, "The Effects of Non-Uniform Mechanical Compression of Lithium-Ion Cells on Local Current Densities and Lithium Plating," *Journal of the Electrochemical Society* 168 (2021): 110515.

13. D. Vidal, C. Leys, B. Mathieu, et al., "Si–C/G Based Anode Swelling and Porosity Evolution in 18650 casing and in Pouch Cell," *Journal of Power Sources* 514 (2021): 230552.

14. J. H. Lee, H. M. Lee, and S. Ahn, "Battery Dimensional Changes Occurring During Charge/Discharge Cycles—Thin Rectangular Lithium Ion and Polymer Cells," *Journal of Power Sources* 119–121 (2003): 833–837.

15. B. Rieger, S. V. Erhard, K. Rumpf, and A. Jossen, "A New Method to Model the Thickness Change of a Commercial Pouch Cell During Discharge," *Journal of the Electrochemical Society* 163 (2016): A1566–A1575.

16. D. Sauerteig, S. Ivanov, H. Reinshagen, and A. Bund, "Reversible and Irreversible Dilation of Lithium-Ion Battery Electrodes Investigated by In-Situ Dilatometry," *Journal of Power Sources* 342 (2017): 939–946.

17. D. Sauerteig, N. Hanselmann, A. Arzberger, H. Reinshagen, S. Ivanov, and A. Bund, "Electrochemical-Mechanical Coupled Modeling and Parameterization of Swelling and Ionic Transport in Lithium-Ion Batteries," *Journal of Power Sources* 378 (2018): 235–247.

18. F. B. Spingler, S. Kücher, R. Phillips, E. Moyassari, and A. Jossen, "Electrochemically Stable In Situ Dilatometry of NMC, NCA and Graphite Electrodes for Lithium-Ion Cells Compared to XRD Measurements," *Journal of the Electrochemical Society* 168 (2021): 040515.

19. P. Daubinger, F. Ebert, S. Hartmann, and G. A. Giffin, "Impact of Electrochemical and Mechanical Interactions on Lithium-Ion Battery Performance Investigated by Operando Dilatometry," *Journal of Power Sources* 488 (2021): 229457.

20. X. Wang, Y. Song, H. Cui, et al., "Insight Into the Electrochemical Behaviors of NCM811|SiO-Gr Pouch Battery Through Thickness Variation," *Energy & Environmental Materials* 6, no. 5 (2023), e12501.

21. Z. Wan, S. Pannala, C. Solbrig, T. R. Garrick, A. G. Stefanopoulou, and J. B. Siegel, "Degradation and Expansion of Lithium-Ion Batteries With Silicon/Graphite Anodes: Impact of Pretension, Temperature, C-Rate and State-of-Charge Window," *eTransportation* 24 (2025): 100416.

22. O. Queisser, L. Cloos, F. Boehm, D. Oehler, and T. Wetzel, "Impact of the Level of Homogenization in 3D Thermal Simulation on the Internal Temperature Distribution of Li-Ion Battery Cells," *Energy Technology* 9, no. 6 (2021), 2000915.

23. A. D. Muresanu and M. C. Dudescu, "Modelling of a Cylindrical Battery Mechanical Behavior Under Compression Load," *Batteries* 10 (2024): 353.

24. K. Higa and V. Srinivasan, "Stress and Strain in Silicon Electrode Models," *Journal of the Electrochemical Society* 162 (2015): A1111–A1122.

25. D. C. Drucker and W. Prager, "Soil Mechanics and Plastic Analysis or Limit Design," *Quarterly of Applied Mathematics* 10 (1952): 157–165.

26. F. L. DiMaggio and I. S. Sandler, "Material Model for Granular Soils," *Journal of the Engineering Mechanics Division* 97 (1971): 935–950.

27. G. Ipers, J. Jiao, S. Pathak, et al., "Rapid Simulation of Electro-Chemo-Mechanical Deformation of Li-Ion Batteries Based on Porous Electrode Theory," *Journal of the Electrochemical Society* 171 (2024): 050557.

28. J. Jiao, E. Kim, W. Li, et al., "Modeling the Powder Plasticity of Porous Electrodes for the Prediction of Battery Breathing and Swelling Prior to Degradation," *Journal of Power Sources* 662 (2026): 238736.

29. D. Schreiner, A. Klinger, and G. Reinhart, "Modeling of the Calendering Process for Lithium-Ion Batteries With DEM Simulation," *Procedia CIRP* 93 (2020): 149–155.

30. M. Sonzogni, J.-M. Vanson, Y. Reynier, S. Martinet, K. Ioannidou, and F. Radjai, "Discrete Modeling of the Calendering Process for Positive Electrodes of Li-Ion Batteries," *Powder Technology* 442 (2024): 119891.

31. M. Lippke, C. Willuhn, T. Ohnimus, et al., "Coupled Numerical Simulation of the Drying and Calendering for Lithium-Ion Battery

21944296, 2026, 11, Downloaded from https://onlinelibrary.wiley.com/doi/10.1002/ente.70723 by Karlsruher Institut Fur Technologie, Wiley Online Library on [13/11/2026]. See the Terms and Conditions (https://onlinelibrary.wiley.com/terms-and-conditions) on Wiley Online Library for rules of use; OA articles are governed by the applicable Creative Commons License

Anodes With Non-Spherical Particles," *Powder Technology* 452 (2025): 120566.

32. J. M. Foster, Y. Hahn, H. Patanwala, V. Oancea, and E. Sahraei, "Mechanical Deformation in Lithium-Ion Battery Electrodes: Modeling and Experiment," *Journal of Electrochemical Energy Conversion and Storage* 22, no. 1 (2024), 011012.

33. Z. Liao, H. Li, H. Wang, and B. Liu, "Mesoscale Mechanical Models for Active Materials in Lithium-Ion Batteries Using the Multi-Particle Finite Element Method," *Extreme Mechanics Letters* 69 (2024): 102154.

34. H. Lin, Y. Wu, B. Lewerich, E. Knobbe, T. Danner, and A. Latz, "Characterization of Elasticity for Silicon-Containing Anodes by Microindentation," *Energy Technology* 13 (2025), 2500383.

35. A. N. Schofield, Critical State Soil Mechanics, (McGraw-Hill, 1968), p. 310.

36. J. Brehm, A. Durdel, T. Kussinger, P. Kotter, M. Altmann, and A. Jossen, "Mechanical Characterization and Modeling of Large-Format Lithium-Ion Battery Cell Electrodes and Separators for Real Operating Scenarios," *Batteries* 10 (2024): 422.

37. Y. Wang, D. Dang, D. Li, J. Hu, and Y.-T. Cheng, "Influence of Polymeric Binders on Mechanical Properties and Microstructure Evolution of Silicon Composite Electrodes During Electrochemical Cycling," *Journal of Power Sources* 425 (2019): 170–178.

38. D. Systèmes, ABAQUS Analysis User's Manual 2025, Providence, 2025.

39. M. GmbH, "GeoDict User Guide," (Math2Market GmbH, 2023).

40. P. Baade, M. Ebner, and V. Wood, "Rapid, Non-Invasive Method for Quantifying Particle Orientation Distributions in Graphite Anodes," *Journal of the Electrochemical Society* 164 (2017): E348–E351.

41. S. Malifarge, B. Delobel, and C. Delacourt, "Quantification of Preferred Orientation in Graphite Electrodes for Li-Ion Batteries With a Novel X-Ray-Diffraction-Based Method," *Journal of Power Sources* 343 (2017): 338–344.

Supporting Information

Additional supporting information can be found online in the Supporting Information section.

Appendix

The appendix outlines the governing equations for the linear contact and the Coulomb friction model employed in the Abaqus particle-resolved simulation framework (step 2 in the workflow). In the particle-resolved simulations, a constant contact stiffness (k) links the normal contact pressure (p) with the local overclosure (h) of the two contact surfaces by

$$p = kh, \tag{7}$$

and k is fixed at 2 GPa in the particle-resolved simulations. Finally, the Coulomb friction model governs the relationship between the maximum allowable shear stress (τ_{crit}) across an interface and the normal contact pressure:

$$\tau_{\text{crit}} = fp, \tag{8}$$

where f is the friction coefficient. Sliding of the surfaces at the local interface is allowed when τ_{crit} is reached. It is worth noting that a separate kinetic friction coefficient is not defined in the particle-resolved simulation framework, meaning that the same coefficient for both static and kinetic friction is assumed. In the DoE, f is set to 0.2, 0.5, and 0.8.

21944296, 2026, 11, Downloaded from https://onlinelibrary.wiley.com/doi/10.1002/ente.70723 by Karlsruher Institut Fur Technologie, Wiley Online Library on [13/11/2026]. See the Terms and Conditions (https://onlinelibrary.wiley.com/terms-and-conditions) on Wiley Online Library for rules of use; OA articles are governed by the applicable Creative Commons License